

VIV analysis of a single elastically-mounted 2D cylinder: Parameter Identification of a single-degree-of-freedom multi-frequency model

Riccardo Pigazzini^a, Giorgio Contento^{a,*}, Simone Martini^a, Thomas Puzzer^a,
Mitja Morgut^a, Andrea Mola^b

^a Department of Engineering and Architecture - University of Trieste, via Valerio 10 34127 Trieste, Italy

^b MathLab, International School for Advanced Studies (SISSA), via Bonomea 265 34139 Trieste, Italy

ARTICLE INFO

Accepted 10 January 2018

Keywords:

VIV
sdof-mf model
Parameter identification
CFD

ABSTRACT

A novel single-degree-of-freedom multi-frequency model (*sdof-mf*) for the prediction of the Vortex Induced Vibrations (VIV) of an elastically mounted circular cylinder in two-dimensional cross flow is presented. The proposed model treats the total hydrodynamic force as sum of conventional Morison-like inertia and drag terms related to the cylinder motion in still fluid plus additional harmonics that account for the lift force induced by vortex shedding. Amplitudes, frequencies and phase lags of these harmonics are identified using a Parameter Identification (*PI*) procedure applied to time domain data of vortex induced forces, here obtained via CFD simulations. The proposed sharp identification via *PI* of the independent frequencies of the vortex shedding fluid force is the peculiarity of the proposed method. The model is assessed considering a wide range of flow regimes, including lock-in conditions. From the overall results, the proposed *sdof-mf* model exhibits promising but consistent capabilities in the reproduction of the vortex shedding forces and cylinder motion, in terms of both amplitudes and frequencies.

1. Introduction

Vortex Induced Vibrations (VIV) of cylinders in cross flow conditions arise in many fields of engineering. The prediction of fatigue damages and ultimate strength are final goals. Among others, coastal and marine applications such as marine cables, subsea pipelines, floating offshore structures and risers are worth mentioning. VIV has been studied and adopted also for energy harvesting, using one or more oscillating cylinders in a sea current. An example of this application is VIVACE converter, a hydro-kinetic power-generating device proposed by Bernitsas et al. (2008).

VIV occurs when vortexes shed by a blunt structure in steady (or unsteady) flow induce an oscillatory force on the structure, mostly in the direction perpendicular to the ambient flow. If the structure is free to move or vibrate in the direction perpendicular to the onset flow or it is partially restrained by restoring forces (moorings, structural stiffness, ...), the body starts oscillating. The quasi-synchronization between vortex shedding frequency and natural frequency – or *lock-in* – may even occur; the structure undergoes near-resonance motions and large displacements are typically observed.

Such vibrations whose amplitude may be of the same order of the size of the body, depend on several parameters, among others Reynolds number, the stiffness of the restoring mechanism, the mechanical damping and the mass of the body related

* Corresponding author.

E-mail addresses: riccardo.pigazzini@phd.units.it (R. Pigazzini), contento@units.it (G. Contento), simone.martini@phd.units.it (S. Martini), tpuzzer@units.it (T. Puzzer), mmorgut@units.it (M. Morgut), andrea.mola@sisssa.it (A. Mola).

to the displaced mass of fluid. There are also additional features that can affect the cylinder response such as the surface roughness and the incoming flow turbulence.

The subject has received huge consideration and a large amount of literature is now available, covering many aspects of the problem. Among others, [Gabbai and Benaroya \(2005\)](#), [Williamson and Govardhan \(2008\)](#) and [Bearman \(2011\)](#) have given a very detailed review of VIV. For further insight on the topic, the reader is redirected to these papers.

VIV is an extremely complex phenomenon, with large variations of the response of the cylinder even for small variations of the magnitude of the incident flow. Bifurcation of the response, i.e. multiple steady amplitudes of oscillation induced by the same ambient flow speed, may take place in case of low mass compared to the displaced fluid mass.

One of the key points that emerges from the literature is the attempt to give a simplified and unified model that could be used at the design stage, typically based on empirical coefficients derived from extensive experimental tests or simulations. Following [Gabbai and Benaroya \(2005\)](#), the semi-empirical models found in the literature can be classified in three main types:

- (i) wake-body coupled models where two coupled equations are set for the body motion and the lift force respectively;
- (ii) single-degree-of-freedom (*sdof*) models where a single equation is set for the body motion and the lift force depends explicitly on the body motion;
- (iii) force-decomposition models where the force is described by a set of coefficients derived from experiments.

Sdof models are simple and effective but still they need care in their application.

As for VIV experiments, [Bearman \(1984\)](#) has given a fundamental review of the experimental studies related to vortex shedding from bluff bodies.

[Khalak and Williamson \(1996\)](#) have conducted a comprehensive experimental campaign on an elastically mounted 2D cylinder with very low mass and damping ratios. The non-dimensional response amplitude of the cylinder has been presented as function of a non-dimensional incident velocity. Their results are considered reference data in the literature.

More recently [Vikestad et al. \(2000\)](#) have presented the results of experimental tests on a 2D elastically mounted cylinder in uniform current and with additional external disturbance, aimed at the evaluation of the added mass as function of the reduced velocity U^* . They assume that the cylinder motion and the vortex induced force are basically both monochromatic. Under this assumption, they came up with showing very large variations of the added mass (even negative) in the reduced velocity range that includes the lock-in region.

A comprehensive review on the fluctuating lift on a cylinder has been given by [Norberg \(2003\)](#), with focus on 3D effects. A new set of measurements has been presented too ([Norberg, 2003](#)), in particular pressure distribution on the cylinder surface.

As for Computational Fluid Dynamics (CFD) simulations, due to the continuously increasing capabilities of both hardware and numerical models/solutions, a considerable number of 2D and 3D CFD results have given a large contribution to the understanding of the VIV problem. Several different models and schemes are adopted to describe the flow field. These include the Discrete Vortex Method (DVM), Large Eddy Simulation (LES), Reynolds Averaged Navier Stokes (RANS) simulations, Direct Numerical Simulation (DNS) or combinations, for example Detached Eddy Simulations (DES). A comprehensive review is given in [Gabbai and Benaroya \(2005\)](#).

In the context of RANS simulations, [Guilmineau and Queutey \(2004\)](#) have used a 2D finite volume RANS code with Menter's $k - \omega$ SST turbulence model. Their study includes three different initial conditions for the flow velocity, starting from rest or varying smoothly and slowly the incident flow, in both increasing and decreasing direction. With such strategy, both the initial branch and the lower branch of the response amplitude ratio could be examined. Still their numerical results do not match perfectly the upper branch found from experiments.

[Pan et al. \(2007\)](#) have used the same $k - \omega$ SST turbulence model and carried out a detailed study on the influence of Reynolds-averaging procedure on the features of the upper branch in the cylinder (riser) response. They explained the absence of the upper branch with the disparity in the random behavior between experiments and the results obtained by RANS codes.

[Wanderley et al. \(2008\)](#) used the $k - \epsilon$ turbulence model. The results obtained agreed very well with experimental data and demonstrated the ability of this methodology in predicting amplitudes for a low mass ratio case.

[Wu et al. \(2014\)](#) have conducted the simulation using the open source CFD tool OpenFOAM with the Spalart-Allmaras turbulence model. Only the *at rest* initial condition has been tested. The results of maximum amplitude ratio, frequency ratio, and vortex pattern compare well with experimental data. Transition between VIV branches is predicted successfully, even though the predicted upper branch is not fully satisfactory: the amplitude ratio is found 5% lower than the corresponding experimental values.

[Kinaci \(2016\)](#) has conducted URANS simulations for Reynolds numbers up to 130.000.

Quite recently, [Mittal and Mittal \(2016\)](#) have conducted a linear stability analysis of the direct time integration of the governing equations in laminar regime ($Re < 200$) via stabilized finite element method.

In the present work, we tackle the problem of 2D 1-DoF VIV in cross-flow direction with low mass and damping ratios. The experimental work by [Khalak and Williamson \(1996\)](#) is used as reference test case. A single-degree-of-freedom multi-frequency *sdof-mf* model for the Vortex Shedding induced force is proposed where a Parameter Identification (*PI*) method is applied in order to compute the unknown parameters of the *sdof-mf*. The proposed model splits the total hydrodynamic force acting on the cylinder in conventional Morison-like inertia and drag terms related to the cylinder motion in calm water and three harmonic terms that account for the lift force induced by vortex shedding. These harmonics are assumed to have no mutual (Fourier) relationship. Their amplitudes, frequencies and phase lags (unknown parameters) can be computed by

tuning the *sdof-mf* model to available data, either experimental or numerical. In this study the parameters are identified by a *PI* procedure in a wide range of the (non-dimensional) incident flow velocity available from the numerical simulations performed in the context of this study. As a first step the simulations are carried out using the URANS solver available in OpenFOAM CFD toolbox (Contento et al., 2015; Lupieri and Contento, 2015, 2017).

From the overall results it emerges that the proposed *sdof-mf* model exhibits promising but consistent capabilities in the reproduction of the vortex shedding forces and cylinder motion, in terms of both amplitudes and frequencies.

The paper is organized as follows.

The test case used as reference data is introduced in Section 2.

The basic physics, the proposed *sdof-mf* model and the Parameter Identification strategy are introduced in Section 3.

An overview of the CFD simulations conducted in this work is given in Section 4.

Finally the results obtained from the simulations and from the *sdof-mf* model are discussed in Section 5.

2. Test case

A circular cylinder, mounted on a linear spring, working in uniform cross flow of velocity U , is considered. Fig. 1 presents a sketch of the system. The study is carried out according to the two-dimensional experimental setup of Khalak and Williamson (1996) where M is the cylinder mass, D the diameter and S the length of the cylinder. K and H are the constants of the linear spring and of the weak linear damper, respectively. ρ and ν are the fluid density and kinematic viscosity respectively.

A wide range of flow regimes, characterized by reduced velocity $U^* = U/(f_0 D)$, is taken into consideration. f_0 is the natural frequency of the system in fluid at rest. The reduced velocity U^* is varied between 2 and 16 approximately, corresponding to sub-critical Reynolds numbers in the range $2.0 \cdot 10^3$ to $1.3 \cdot 10^4$. It is worth noting that in the work of Khalak and Williamson (1996) U^* is defined according to the natural frequency in air $f_{0,air}$, where the added mass is three orders of magnitude smaller than in water. Their U^* values have been recomputed here, for fresh water.

Khalak and Williamson (1996) conducted the experiments at the Cornell-ONR free-surface water channel with a vertical surface-piercing cylinder. The entire set of velocities of the onset flow at a given U^* was obtained with smooth continuous increment of the relative incident flow velocity, from the lowest to the highest. A fixed flat horizontal plate was installed at a $0.04D$ from the bottom of the cylinder in order to minimize 3D effects at the bottom end of the cylinder.

Morse et al. (2008) studied the effect of the end conditions (with or without end plates at the far end or small gaps with a fixed bottom) concluding that unless the gap exceeds a given threshold, the results are almost comparable. Thus we have assumed that those data can be considered 2D.

The mass/damping data used in the experiments and in the present simulations are such that the problem is characterized by low mass ratio $m^* = 2.4$ and low damping $\zeta = H/H_{critical} \approx 0.0054$ ratios. The study is performed using fresh water. Table 1 summarizes definitions and data.

3. Mathematical model

The governing equations of the proposed single-degree-of-freedom multi-frequency *sdof-mf* model are presented first.

Afterward, the Parameter Identification (*PI*) strategy used to compute the unknown parameters of the *sdof-mf* model is outlined.

The *PI* methodology is completely general and could be applied to any experimental or numerical VIV time-domain data.

3.1. Cylinder dynamics and *sdof-mf* model

According to the system sketched in Fig. 1, the cylinder motion (one degree of freedom, 1 DoF) in fluid at rest can be modeled as:

$$M \ddot{y} + H \dot{y} + K y = F_{SF}(t) \quad (1)$$

$F_{SF}(t)$ is the hydrodynamic force in still fluid (*SF*).

It is recognized (Sarpkaya and Isaacson, 1981; Morison et al., 1950) that $F_{SF}(t)$ can be expressed consistently and accurately as the sum of Morison-like inertia and quadratic drag terms (Eq. (2)).

$$F_{SF}(t) = -M_A \ddot{y} - Q \dot{y} |\dot{y}|. \quad (2)$$

In the above equation $M_A = C_A \rho \frac{\pi D^2}{4} S$ is the added mass, where C_A is the added mass coefficient. Q is given by $Q = \frac{1}{2} C_D \rho D S$, where C_D is the drag coefficient.

After substitution, Eq. (1) becomes:

$$(M + M_A) \ddot{y} + H \dot{y} + Q \dot{y} |\dot{y}| + K y = 0. \quad (3)$$

Adopting the energy balance method under the assumption of a quasi-steady state harmonic response of amplitude A and frequency ω , the equivalent linear drag Q_{eq} is easily computed as $Q_{eq} = \frac{8}{3\pi} Q \omega A$ so that Eq. (3) can be rewritten as

$$(M + M_A) \ddot{y} + (H + Q_{eq}) \dot{y} + K y = 0 \quad (4)$$

C_A and C_D can be derived from consolidated experimental data according to the Keulegan-Carpenter and Reynolds numbers of the specific system (Sarpkaya and Isaacson, 1981).

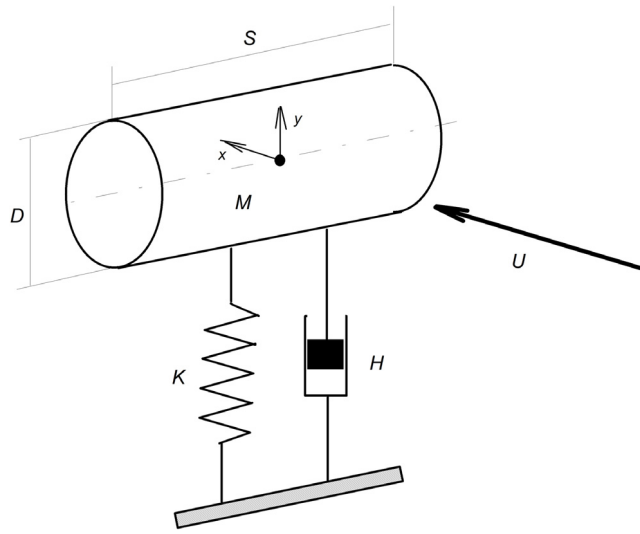


Fig. 1. Schematic representation of VIV problem and relevant symbols.

Table 1
System properties.

Description	Symbol	Value
Cylinder diameter	D (m)	0.0381
Cylinder length	S (m)	0.0250
Cylinder mass	M (kg)	0.0683
Spring stiffness	K (N/m)	1.6609
Structural damping	H (N/(m/s))	0.0043
Mass ratio	$m^* = M/(\rho \frac{\pi D^2}{4} S)$	2.4000
Damping ratio	$\zeta = H/(2\sqrt{K(M + M_A)})$	0.0054
Adopted added mass coeff.	$C_A = M_A/(\rho \frac{\pi D^2}{4} S)$	1.0000
Mass-damping parameter	$m^* \zeta$	0.0130
Natural frequency in air	$f_{0, air}$ (Hz)	0.7846
Natural frequency in water	f_0 (Hz)	0.6592

In the presence of current U , Eq. (1) is modified in order to include the additional force $F_{VS}(t)$ that arises from the vortex shedding (VS) process. Thus Eq. (1) turns into Eq. (5)

$$M \ddot{y} + H \dot{y} + K y = F_{SF}(t) + F_{VS}(t) \quad (5)$$

and the substitution of Eq. (2) in Eq. (5) leads to

$$(M + M_A) \ddot{y} + H \dot{y} + Q \dot{y} | \dot{y} | + K y = F_{VS}(t). \quad (6)$$

Assuming that the added mass and drag coefficients are known a priori or from specific tests (free decay or forced oscillations), the splitting of the total force in standard inertia/drag $F_{SF}(t)$ and vortex shedding $F_{VS}(t)$ terms, i.e. $F_{TOT}(t) = F_{SF}(t) + F_{VS}(t)$, allows to examine in details the RHS of Eq. (6).

At this stage, it is important to point out that, as first approximation, the force and/or the response might be assumed monochromatic (Khalak and Williamson, 1996). This is true in most of the U^* range, with some distinctions. Nevertheless (see Fig. 4 later on), it seems that the approximation of the vortex shedding force $F_{VS}(t)$ could be considerably improved considering the contribution of a larger number of harmonics. For the improvement to be effective, the additional requirement is that these frequencies must be totally independent from each other (not Fourier dependent). In non-dimensional form, $F_{VS}(t)$ can be written conveniently as:

$$\begin{aligned} \frac{F_{VS}(t)}{F_0} &= C_{L, VS}(t) \approx \overline{C_{L, VS_1}} \sin(2\pi \cdot \theta_1 \cdot f_{St} \cdot t + \phi_1) \\ &+ \overline{C_{L, VS_2}} \sin(2\pi \cdot \theta_2 \cdot f_{St} \cdot t + \phi_2) \\ &+ \overline{C_{L, VS_3}} \sin(2\pi \cdot \theta_3 \cdot f_{St} \cdot t + \phi_3) \end{aligned} \quad (7)$$

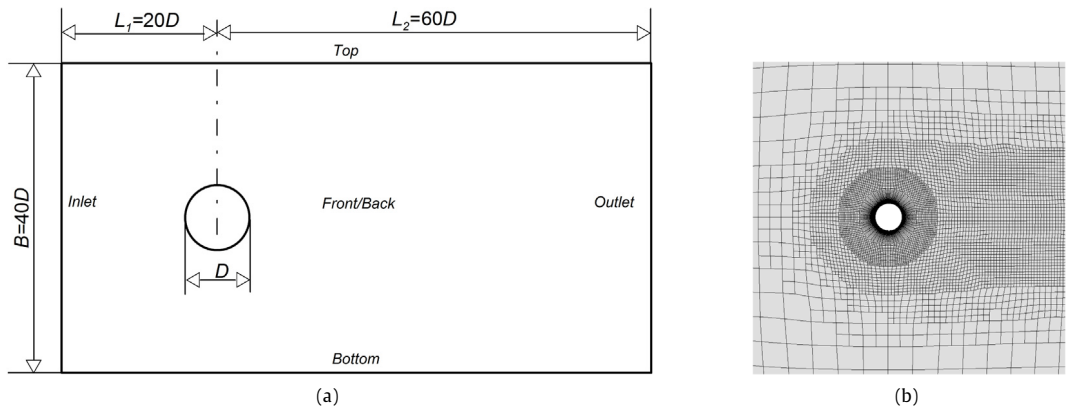


Fig. 2. Computational domain (a) and details of the grid refinement in the near-wall region (b).

where $F_0 = \frac{1}{2}\rho DSU^2$ is a reference force and $f_{St} = St \cdot U/D$ is the Strouhal frequency ($St =$ Strouhal number). $\overline{C_{L,VS_i}}$, θ_i and ϕ_i ($i = 1, 3$) are nine unknown parameters. They are assumed to be functions of U^* . In the following the RHS of Eq. (7) is identified in compact form as $C_{L,VS_{mf}}(t)$. The subscript *mf* stands for *multi-frequency model*.

3.2. Parameter identification

For a given U^* and for a sufficiently long time series obtained from experimental measurements or CFD simulations, a subset (*stationary time window*) of the time record can be selected for the analysis. In this subset the stationary harmonic condition of the cylinder motion and related forces must be reasonably fulfilled.

For that U^* and that time-series subset:

- (i) Eqs. (6) and (7) describe the stationary (frequency-domain) part of the fluid–body interaction due to vortex shedding;
- (ii) the nine unknown parameters ($\overline{C_{L,VS_i}}$, θ_i , ϕ_i ($i = 1, 3$)) can be assumed to be constant (time independent).

Since the vortex shedding component $F_{VS}(t)$ can be computed as $F_{VS}(t) = F_{TOT}(t) - F_{SF}(t)$, the LHS of Eq. (7) is known (from experiments or simulations) and a least-square fitting can be applied to the RHS of Eq. (7) to determine the unknown parameters (*PI*). Thus, for any U^* obtained with simulations or experiments, given N_s time-domain samples of the vortex shedding non-dimensional force $C_{L,VS}(t_j)$, the best fit model can be found setting χ^2 to its minimum, where:

$$\chi^2 = \sum_{j=1, N_s} [C_{L,VS}(t_j) - C_{L,VS_{mf}}(t_j)]^2. \quad (8)$$

The Levenberg–Marquardt iterative algorithm (Levenberg, 1944; Marquardt, 1963; Press et al., 1992) is here used for the purpose.

4. Overview of the CFD simulations

In this study, VIV time series used to identify the unknown parameters of the *s dof-mf* model have been obtained via URANS-based CFD simulations. It is worth mentioning that the complexity of the phenomenon (3D nature, detached flow, turbulence, ...) would probably require more sophisticated and computationally demanding numerical models, mostly in a narrow range of U^* around the peak of the response of the cylinder. An enhanced CFD solution is left to a further stage of this study, here focused on the presentation and evaluation of the applicability of the proposed *s dof-mf* model with *PI*.

Under these premises, the computations have been performed using the URANS approach, in combination with the workhorse Shear Stress Transport turbulence model. The accuracy of the expected and obtained numerical results has been assumed adequate for this first-step investigation (*s dof-mf* + *PI*).

The numerical simulations have been performed using the OpenFOAM (*OF*) library (release 2.4), an open-source finite-volume-based CFD toolbox.

The shape of the computational domain used in the current 2D simulations is sketched in Fig. 2(a), with names of the boundary patches. The computational mesh has 31 282 cells with $y^+ \approx 1$, with a single cell in the direction perpendicular to the plane $O(x, y)$. The number of cells and refinement were determined by a preliminary mesh independence study. Fig. 2(b) shows the mesh refinement close to the cylinder surface.

In Tables 2–4, the boundary and initial conditions used for the velocity, pressure, turbulent kinetic energy k and the turbulence specific dissipation rate ω are listed, along with their mathematical formulations. Bold symbols refer to vectors, “**n**” is the outward unit vector normal to the boundary. The values of k and ω have been computed following Menter’s approach (Menter, 1994).

Table 2
Boundary and initial conditions—Velocity.

Domain/Boundaries	Equation	
	<i>Boundary condition</i>	
Top/Bottom	zeroGradient	$(\mathbf{n} \cdot \nabla \mathbf{u}) = 0$
Inlet	fixedValue	$\mathbf{u} = \mathbf{u}_\infty$
Outlet	inletOutlet	$(\mathbf{n} \cdot \nabla \mathbf{u}) = 0$ if: $\mathbf{u} \cdot \mathbf{n} > 0$ $\mathbf{u} = 0$ if: $\mathbf{u} \cdot \mathbf{n} < 0$
Cylinder wall	movingWallVelocity	$\mathbf{u} = \mathbf{u}_{wall}$
	<i>Initial condition</i>	
Inner domain & Inlet	$\mathbf{u}_\infty = (U, 0, 0)$	

Table 3
Boundary and initial conditions—Pressure.

Domain/Boundaries	Equation	
	<i>Boundary condition</i>	
Top/Bottom	zeroGradient	$(\mathbf{n} \cdot \nabla p) = 0$
Inlet	zeroGradient	$(\mathbf{n} \cdot \nabla p) = 0$
Outlet	fixedValue	$p = p_0$
Cylinder wall	zeroGradient	$(\mathbf{n} \cdot \nabla p) = 0$
	<i>Initial condition</i>	
Inner domain & Outlet	$p_0 = 0$	

Table 4
Boundary and initial conditions— $(k - \omega)$.

Domain/Boundaries	Equation	
	<i>Boundary condition</i>	
Top/Bottom	zeroGradient	$(\mathbf{n} \cdot \nabla k) = 0$ $(\mathbf{n} \cdot \nabla \omega) = 0$
Inlet	fixedValue	$k = k_{far\ field}$ $\omega = \omega_{far\ field}$
Outlet	inletOutlet	$(\mathbf{n} \cdot \nabla k) = 0$ if: $\mathbf{u} \cdot \mathbf{n} > 0$ $k = k_{far\ field}$ if: $\mathbf{u} \cdot \mathbf{n} < 0$ $(\mathbf{n} \cdot \nabla \omega) = 0$ if: $\mathbf{u} \cdot \mathbf{n} > 0$ $\omega = \omega_{far\ field}$ if: $\mathbf{u} \cdot \mathbf{n} < 0$
Cylinder wall	fixedValue	$k = 0$ $\omega = \frac{60\nu}{0.075y_1^2}$
	<i>Initial condition</i>	
Inner domain & Inlet	$k_{far\ field} = 0.1 \frac{U^2}{Re_L}$ $\omega_{far\ field} = 10 \frac{U}{L}$	

Table 5
Schemes in use.

Operator	Symbol	Scheme	Order
Gradient	∇	Linear	2nd
Divergence	$\nabla \cdot (\phi, V)$	Linear upwind	2nd
Laplacian	∇^2	Linear limited	2nd

The *empty* constraint condition of OF has been applied on the *Front* and *Back* patches in order to enforce the two dimensional flow. This condition specifies that the field equations are not solved in the direction perpendicular to these patches.

As far as the body motion is concerned, the ALE method, available in OpenFOAM, has been used to follow the mesh motion (Löhner and Yang, 1996), where the displacement of the internal nodes is computed from the boundary motion by means of the Laplace equation with variable diffusivity based on inverse distance (Löhner and Yang, 1996). The time dependent simulations were carried out using the first order implicit Euler scheme. The other discretization schemes employed in this study are collected in Table 5.

5. Results and discussion

Some representative results of the CFD simulations are given in paragraph 5.1 first. Then, the results obtained with the *s dof-mf* model together with the application of the Parameter Identification are discussed in paragraph 5.2.

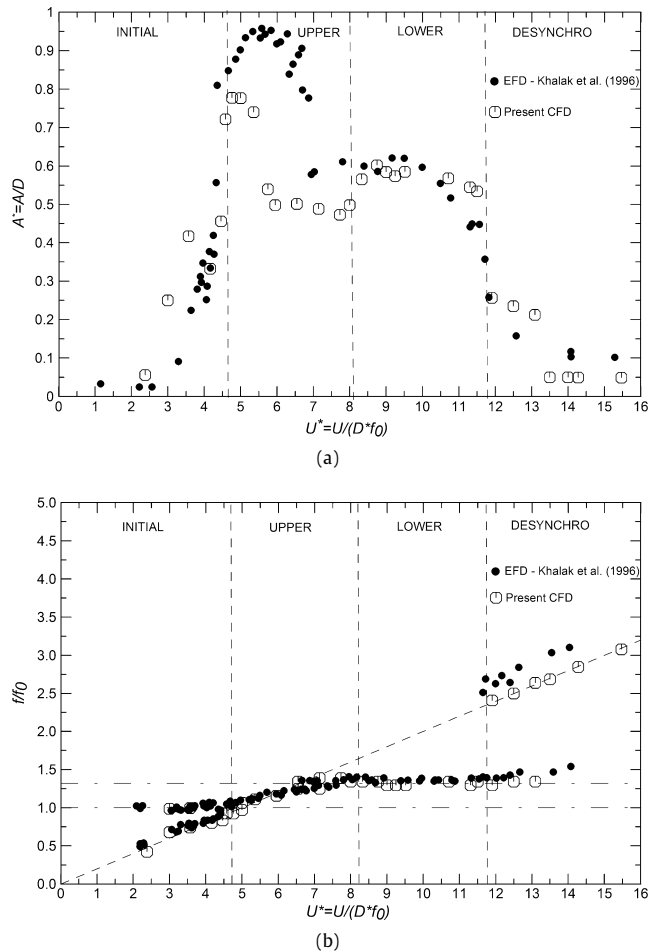


Fig. 3. Amplitude ratio $A^* = A/D$ (a) and frequency ratio $f^* = f/f_0$ (b) versus reduced velocity U^* . Comparison between experimental data by [Khalak and Williamson \(1996\)](#) (●) and present CFD results (○). $m^* = 2.4$. The oblique dashed line in (b) corresponds to the Strouhal frequency (nominal Strouhal number = 0.20).

5.1. Preliminary

The non-dimensional amplitude of the motion of the cylinder $A^* = A/D$ and the non-dimensional dominant frequency of the motion $f^* = f/f_0$ are shown in [Fig. 3\(a\)](#) and [\(b\)](#) respectively. The present CFD results are compared with the experimental data by [Khalak and Williamson \(1996\)](#).

As a preliminary comment, the main features of the cylinder dynamics are reasonably captured. The under-prediction of the cylinder motion in the rightmost part of the upper branch is evident and there is room for improvement using more sophisticated CFD techniques. The results achieved so far within a computationally cheap URANS approach are considered good enough for the main purposes of this first-step study, focused on the development and analysis of the *s dof-mf*.

The computed amplitude A^* shows a pronounced peak at $U^* \approx 5$ (upper branch), an almost constant flat response for U^* between 7 and 11 (lower branch), and very low amplitudes for U^* smaller than 3 (initial branch) and larger than 12 (desynchronization). The steep jumps at $U^* \approx 5.5$ and at $U^* \approx 12$ are well reproduced.

[Fig. 3\(b\)](#) shows the frequency ratio $f^* = f/f_0$ versus the reduced velocity U^* , according to FFT analysis of the cylinder displacement. Frequencies f associated to the two main peaks of the amplitude spectrum are shown. For $U^* < 4.76$ a double peak behavior is found, the lower being the Strouhal frequency, the upper being the natural frequency in still water. For $U^* > 7.73$ the frequency ratio seems to be no longer dependent on U^* and it flattens out around $f/f_0 \approx 1.35$. This is a known behavior at lock-in ([Khalak and Williamson, 1996](#)). Some authors ([Vikestad et al., 2000](#)) ascribe this increment of the natural frequency to a lower value of the added mass. In our view, comparing the hydrodynamic forces that arise in free oscillation of the cylinder in calm water condition (not shown) and in incident flow, vortex shedding introduces a new transverse force. Depending on the value of U^* , this force can be in anti-phase with the inertia term of [Eq. \(2\)](#), thus giving an overall effect that leads to an apparent reduction (even to negative values) of the added mass. In another context, a similar situation occurs in

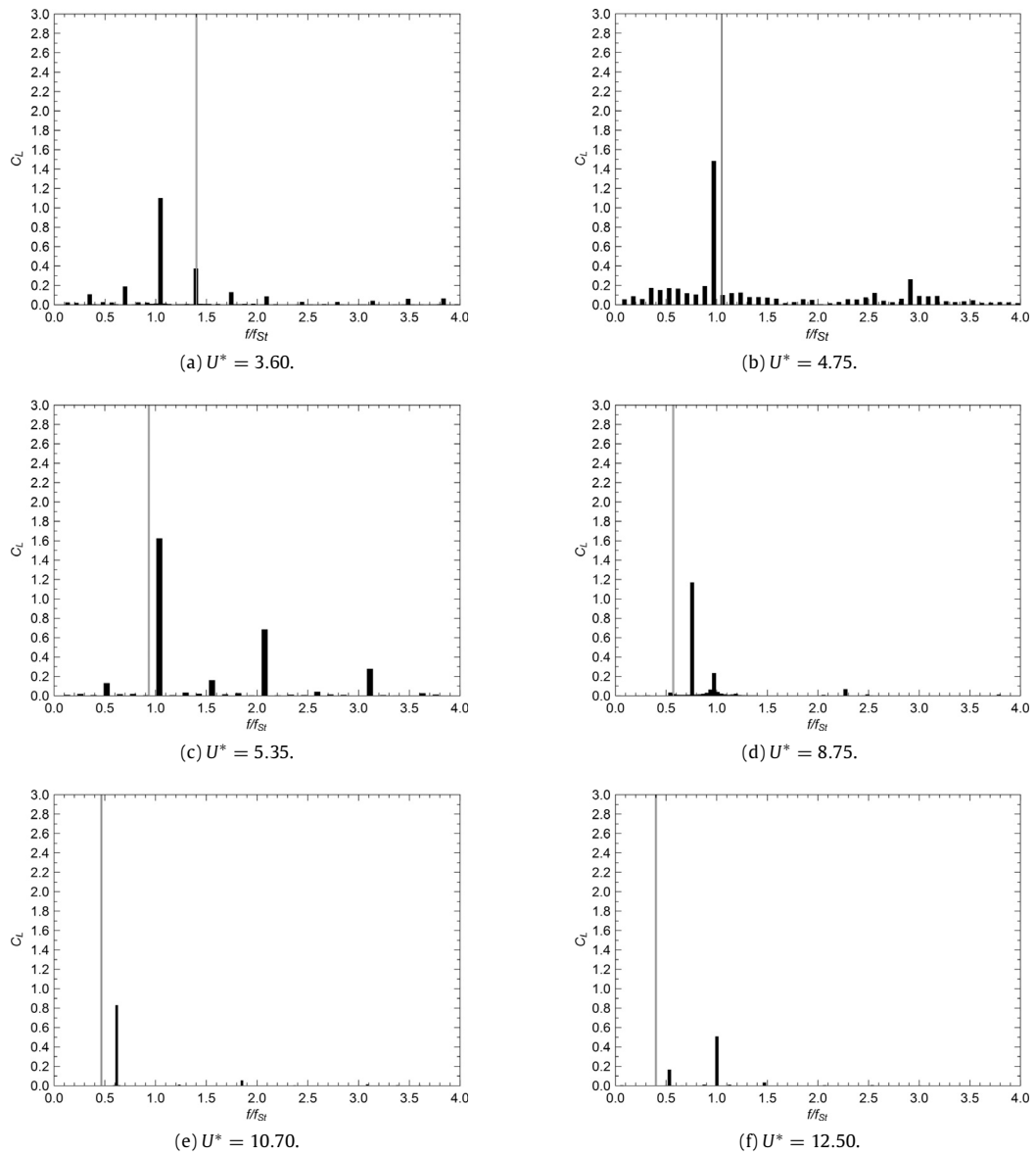
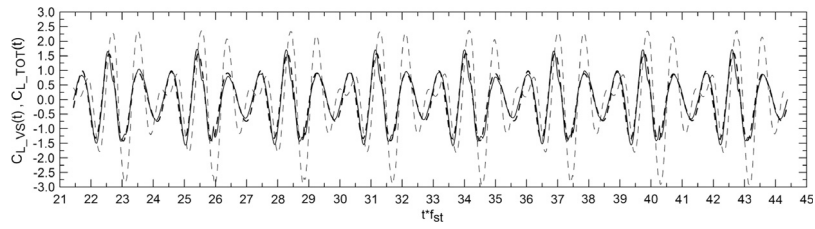


Fig. 4. Amplitude spectra of the non-dimensional vortex shedding force $F_{VS}(t)/F_0$ versus non-dimensional frequency f/f_{St} . Spectral analysis is conducted on the stationary part of the signal (without transient effects). Vertical lines correspond to the non-dimensional natural frequency f_0/f_{St} .

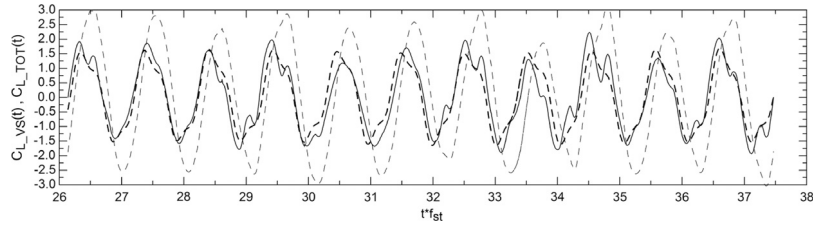
a 2D wavy flow passing a horizontal circular cylinder underneath the free surface, at low Keulegan–Carpenter (KC) numbers (Lupieri and Contento, 2017; Chaplin, 1984; Contento and Codiglia, 2001) ($KC < 2.5$). In that case the inertia term of Morison equations C_M changes its value from the standard $C_M = 2$ to $C_M = 1$ or even less, due to a steady rotating streaming of the boundary layer that induces a Magnus effect in anti-phase with the Morison inertia term. The global result is the apparent reduction of the inertia coefficient C_M whereas it is simply the result of the superposition of two different forces of very different origins.

Back to the present results, as the reduced velocity U^* enters the range $11.899 < U^* < 13.089$, f^* splits into two branches, the lower being 1.35 as for lower U^* , the upper being the Strouhal frequency. This sudden increase in oscillation frequency is accompanied by a rapid drop of the amplitude of oscillation and it is related to the end of synchronization range.

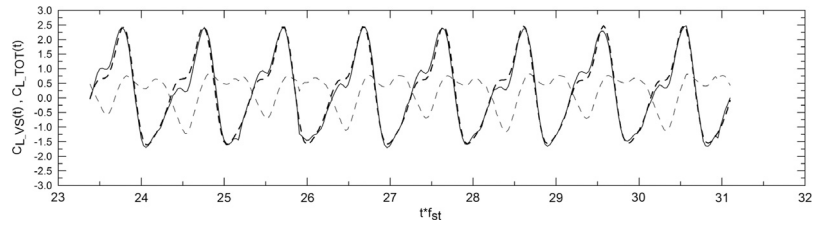
As a general comment, the CFD simulations give an upper branch of A^* that is narrower than the experimental one, i.e the solution jumps to the lower branch quite rapidly for increasing U^* . In the rest of the U^* domain, the present results agree reasonably well with the available experimental data and mostly are in line with the results reported by other authors using a similar computational URANS approach (Guilmineau and Queutey, 2004; Pan et al., 2007; Wanderley et al., 2008; Wu et al., 2014; Kinaci, 2016).



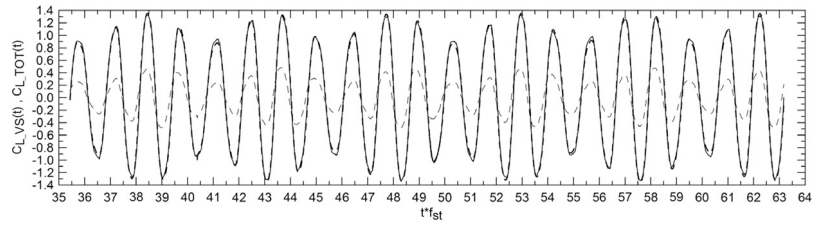
(a) $U^* = 3.60$.



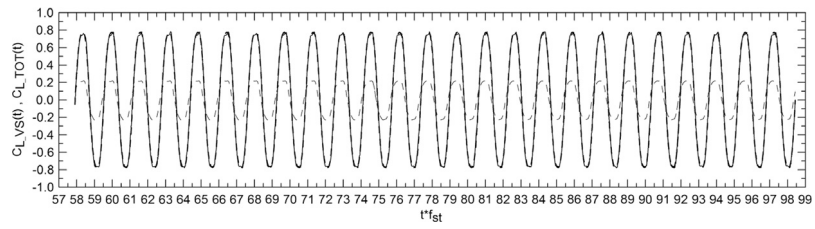
(b) $U^* = 4.75$.



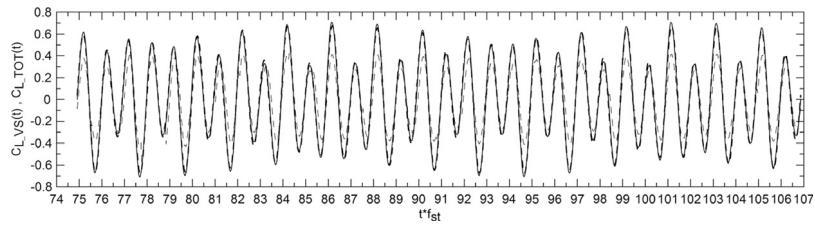
(c) $U^* = 5.35$.



(d) $U^* = 8.75$.



(e) $U^* = 10.70$.



(f) $U^* = 12.50$.

Fig. 5. Time series of the non-dimensional total $C_{L,TOT}(t)$ and vortex shedding $C_{L,VS}(t)$ force for a given U^* . Dashed thin line = total force (present CFD); solid line = vortex shedding force (present CFD); dashed thick line = *sdoF-mf* model (Eqs. (6), (7)).

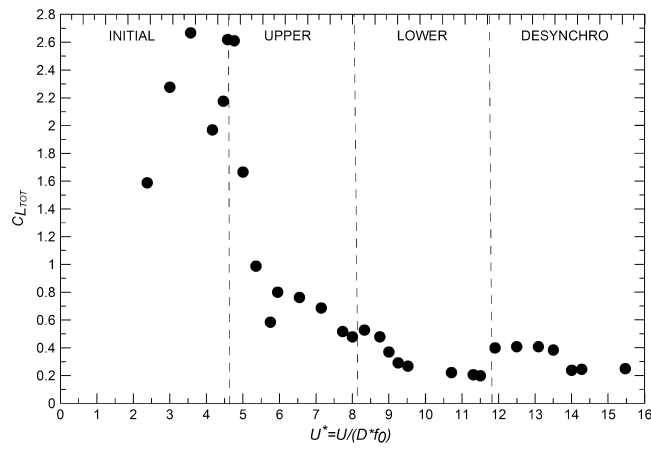


Fig. 6. Non-dimensional amplitude of the total hydrodynamic force $F_{TOT}(t)$. The amplitude is here defined as the average between the absolute values of maxima and minima of $F_{TOT}(t)/F_0$ in the time domain, at steady state.

A source of discrepancy at the upper branch between the present numerical simulations and the experimental data is related to numerical issues which could be improved with more sophisticated CFD simulations.

As for the hysteretic behavior of the motion of the cylinder, not well captured by the present simulations, it is well known that the bifurcation of the response of a non-linear system, i.e. its attitude to get to different solutions under the same forcing term, is strongly dependent on the initial conditions (see for instance [Francescutto and Contento, 1999](#) for the problem of ship rolling). The analysis of the domains of attraction is fundamental ([Guilmineau and Queutey, 2004](#)) but the computational effort may be extremely large if the model that represents the system is complex. In this case, both initial conditions of the cylinder kinematics and the initial conditions of the ambient flow should be taken into consideration.

Summarizing, even though there is large room for improvement, the current computed VIV time series can be assumed as a reference data for a first-step analysis conducted with the proposed *s dof-mf* model and *PI*.

5.2. *S dof-mf* model and parameter identification

With reference to Eqs. (6) and (7), the results discussed in the following were obtained assuming standard values of the added mass/drag coefficients and a standard value of the Strouhal number for sub-critical regime, i.e. $C_A = 1.0$, $C_D = 1.6$ and $S_t = 0.2$ ([Sarpkaya and Isaacson, 1981](#); [Morison et al., 1950](#)).

According to this standard setup of Eqs. (6) and (7), the following results were obtained.

In [Fig. 4](#) the amplitude spectra of $F_{VS}(t)$ is shown for six representative flow regimes, namely $U^* = 3.60, 4.75, 5.35, 8.75, 10.70, 12.50$. CFD data are analyzed at harmonic steady state, i.e. without transient effects induced by the warm-up of the simulation, either physical or numerical.

[Fig. 5](#) compares the non-dimensional time-domain vortex shedding force obtained with CFD simulations and with the *s dof-mf* model. They refer to the same values of U^* used in [Fig. 4](#). Solid thin lines represent CFD data $C_{L,VS}(t)$, dashed thick lines represent the *s dof-mf* model $C_{L,VS_{mf}}(t)$; for sake of completeness, dashed thin lines represent the total force $C_{L,TOT}(t) = F_{TOT}(t)/F_0$.

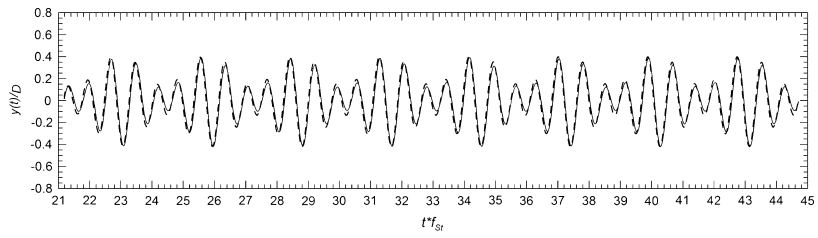
From both spectral ([Fig. 4](#)) and time-domain ([Fig. 5](#)) analyses, it is evident that vortex-shedding force $F_{VS}(t)$ is not well suited for a monochromatic model for any U^* , whereas it can be approximated well by three harmonics in the whole U^* range investigated. However, the peak frequencies of these harmonics look totally independent from each other so that a standard frequency analysis does not allow to identify the frequency values sharply.

As a reminder for the rest of the discussion, [Fig. 6](#) shows the non-dimensional amplitude of the total hydrodynamic force $F_{TOT}(t)$. Since the time series of $F_{TOT}(t)$ is generally everything but monochromatic, the amplitude is here defined as the average between the absolute values of maxima and minima.

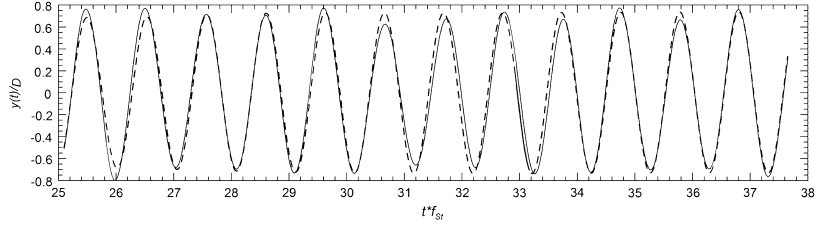
[Fig. 7](#) shows the non-dimensional cylinder displacement versus non-dimensional time, for the same values of U^* used in [Figs. 4](#) and [5](#). Due to their representativeness, [Fig. 8](#) shows five additional cases ($U^* = 3.00, 5.95, 6.54, 13.10, 13.50$). Solid thin lines represent CFD data, dashed thick lines represent the time integral of the *s dof-mf* model, using Eqs. (6) and (7).

From [Figs. 5\(a\)](#) to [8\(e\)](#), it can be observed that the proposed *s dof-mf* model captures/reproduces the vortex shedding force and consequently the cylinder motion very well, even for complex cylinder response ([Fig. 8\(a\)](#)–[\(e\)](#)). The worst fitting of the force is shown in [Fig. 5\(b\)](#). It refers to $U^* = 4.75$. Still the cylinder displacement obtained with the *s dof-mf* at that U^* is rather good ([Fig. 7\(b\)](#)).

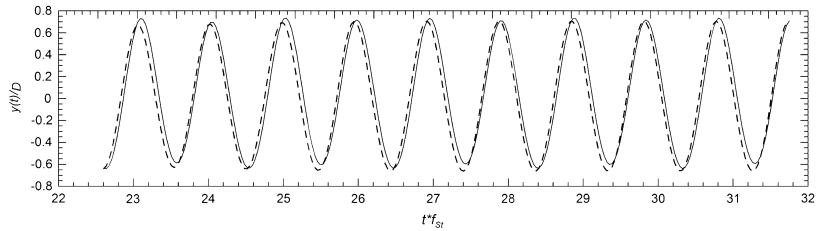
[Fig. 9\(a\)](#) and [\(b\)](#) show the behavior of the non-dimensional amplitudes and frequencies of $F_{VS}(t)$, namely $\overline{C_{L,VS_i}}$ and $(f/f_0)_i = \theta_i \cdot f_{St}/f_0$ ($i = 1, 3$) versus U^* respectively.



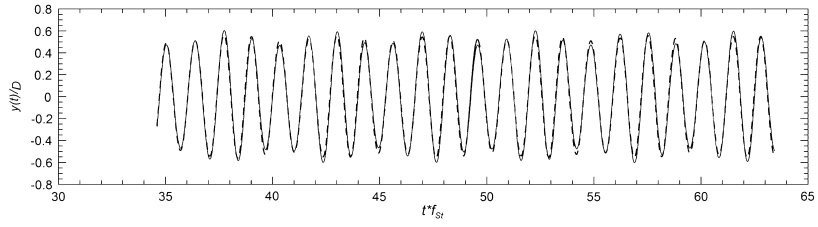
(a) $U^* = 3.60$.



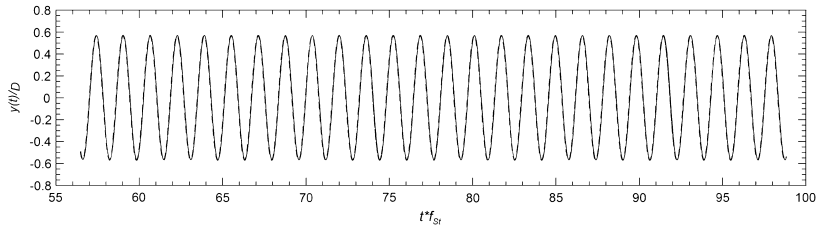
(b) $U^* = 4.75$.



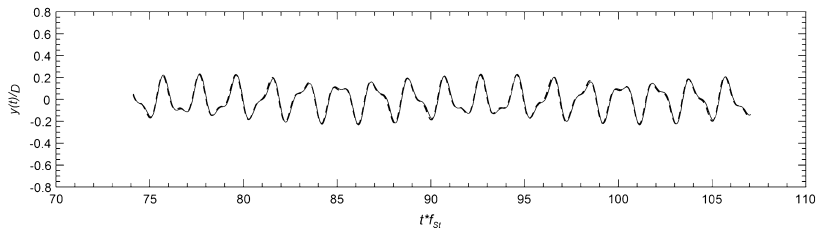
(c) $U^* = 5.35$.



(d) $U^* = 8.75$.



(e) $U^* = 10.70$.



(f) $U^* = 12.50$.

Fig. 7. Time series of the non-dimensional cylinder motion for a given U^* . Solid line = present CFD; dashed thick line = *s dof-mf* model (Eqs. (6), (7)).

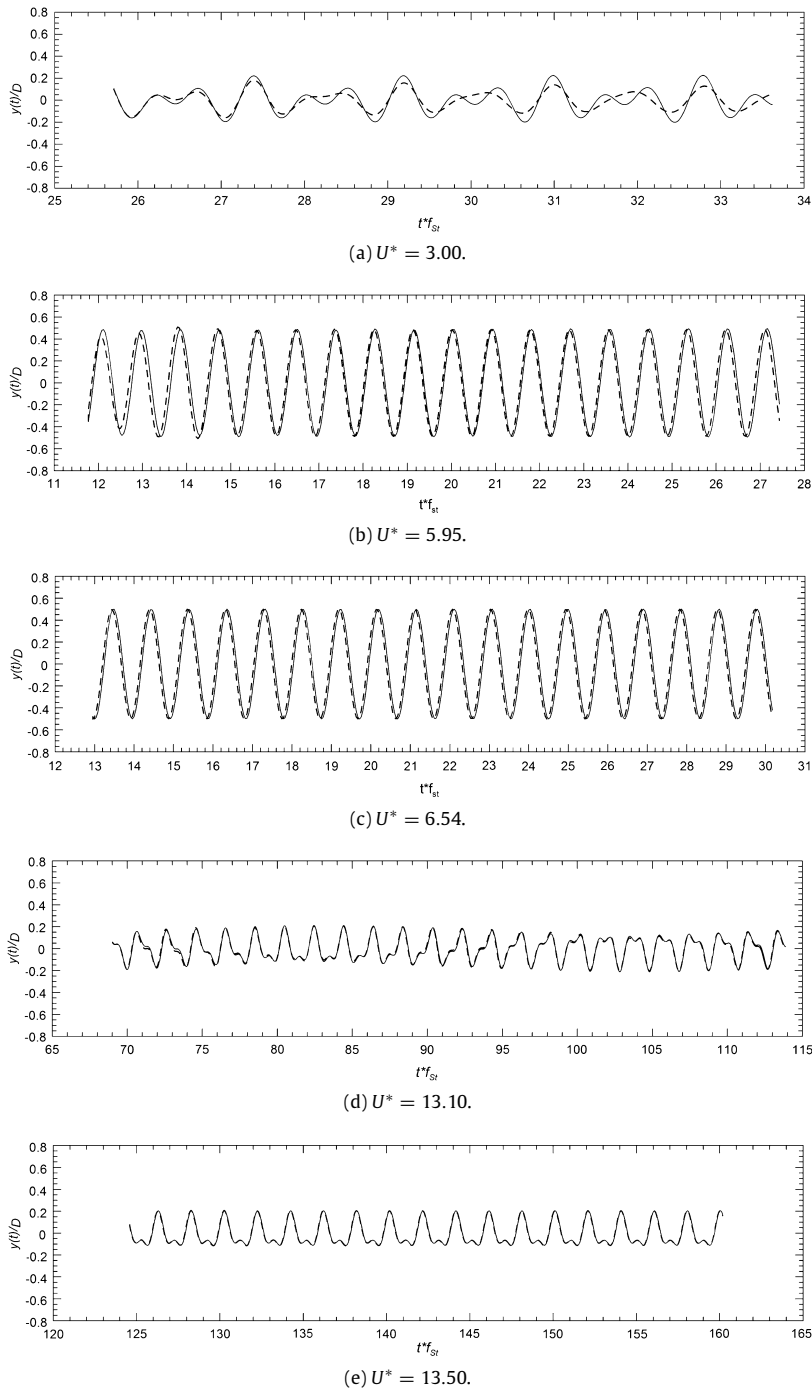
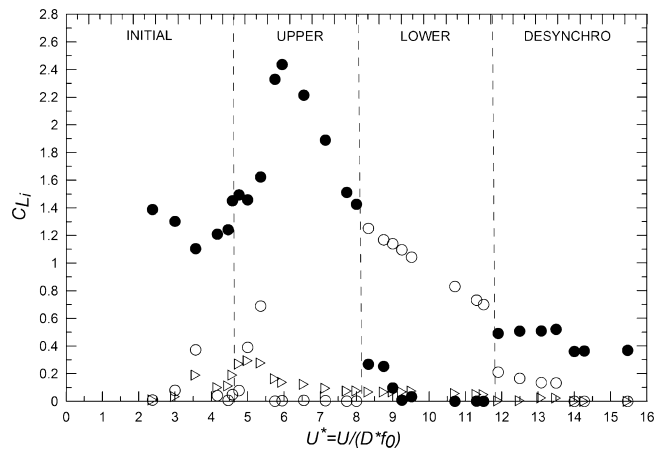


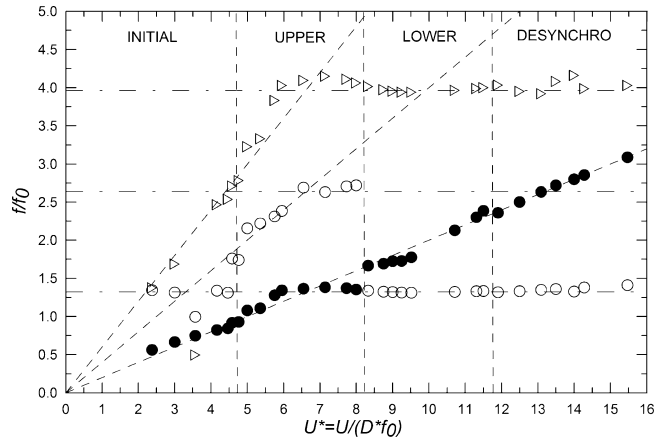
Fig. 8. Time series of the non-dimensional cylinder motion for a given U^* . Solid line = present CFD; dashed thick line = *s dof-mf* model (Eqs. (6), (7)).

From these plots, $F_{VS}(t)$ exhibits a basically monochromatic behavior, with dominant frequency that switches back-and-forth between Strouhal and *lock-in* frequencies. The additional two frequencies may be particularly pronounced, in particular in the transient zones of U^* , where the response of the cylinder changes domain of attraction (jump of amplitude A^*) and the response of the cylinder is large and complex.

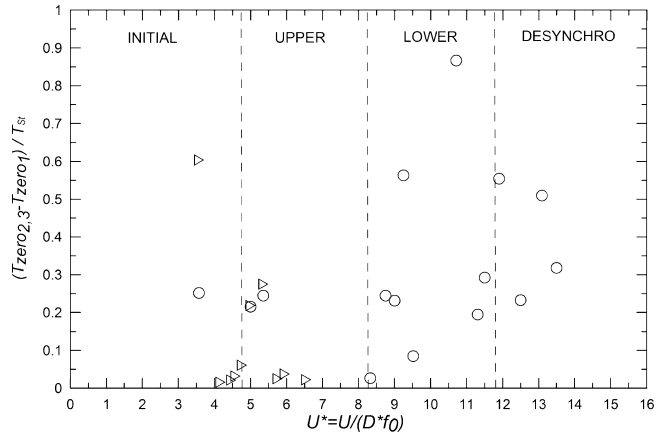
In Fig. 9(a) and (b), the parameters obtained are collected and presented according to the characteristic frequency. Solid circles correspond to the term closest to the Strouhal frequency in the entire U^* range investigated (from now on labeled



(a)



(b)



(c)

Fig. 9. Parameters of the *s dof-mf* model versus U^* . (\bullet) = closest term to the Strouhal frequency in the entire U^* range investigated (C1). (\circ) = term related to the *lock-in* frequency or the double Strouhal frequency (C2). (\triangleright) = term related to the triple Strouhal frequency or the triple lock-in frequency (C3).

as component C1 of $F_{VS}(t)$). Empty circles (component C2) correspond to the *lock-in* frequency term or, as long as the upper branch of the response exists in the range $4.5 < U^* < 8$, it behaves as the double Strouhal frequency. Finally triangles (component C3) correspond to the triple Strouhal frequency up to $U^* \approx 8$. For higher U^* values, this frequency flattens out at the triple *lock-in* frequency.

In general, amplitudes $\overline{C_{L,VS_i}}$ and frequencies $(f/f_0)_i$ of the *s dof-mf* model show an extremely fair and consistent behavior with U^* .

The data presented in Fig. 9(c) are the phase lags of component C2 and C3 related to component C1. They are computed according to the time lag between two adjacent zero crossing up and using the Strouhal period as time scale, as follows

$$\psi_{2,3} = \frac{t_{zeroupC2,3} - t_{zeroupC1}}{T_{St}}. \quad (9)$$

It is worth noting that phase lags become important where the corresponding amplitudes $\overline{C_{L,C2}}$ or $\overline{C_{L,C3}}$ are non negligible, typically in the transient zones of U^* , as discussed above. In these regions, $\psi_{2,3}$ can be well approximated by $\psi_{2,3} \approx 0.25$. Outside these regions, $\psi_{2,3}$ can be set to any value since the corresponding amplitudes are negligible.

As a general comment, the *s dof-mf* model reproduces quite well both forces and cylinder motion. As expected, there is a dominant frequency, either Strouhal or *lock-in* frequency, that provides the bulk of forces and motion. However, lower and higher harmonics give a fundamental contribution, mostly in the transient regimes between one domain of attraction to the next where the multi-frequency behavior is evident.

6. Concluding remarks

Vortex Induced Vibrations (VIV) of an elastically-mounted 2D circular cylinder in cross flow with low mass and damping ratios, have been analyzed in the frame of a single-degree-of-freedom multi-frequency (*s dof-mf*) model. VIV data have been obtained by 2D URANS-based CFD simulations. The results of the numerical simulations have been compared with experimental and numerical data from the literature, justifying the adoption of these data for this first-step development of the *s dof-mf* model and analysis of the results. The *s dof-mf* model proposed splits the total hydrodynamic force acting on the cylinder in standard Morison-like inertia/drag terms and three harmonics. The former is related to the cylinder motion in still fluid, the latter accounts for the lift force induced by vortex shedding. Standard values of added mass and drag coefficients are used. A Parameter Identification (*PI*) method, applied in the time domain to VIV data, allowed to obtain amplitudes, frequencies and phases of the *s dof-mf* model. The unknown parameters obtained via *PI* show a fair and consistent variation with U^* over the entire range investigated. The current *s dof-mf* model exhibits rather promising capabilities in the reproduction of the vortex shedding forces and cylinder motion, in terms of both amplitudes and frequencies, even in complex detached flow conditions. In order to improve the current *s dof-mf* model, the ongoing work is twofold: (i) the adoption of more sophisticated CFD simulations that should overcome the problems encountered by the URANS method; (ii) the application of the *s dof-mf* model to extensive data, either experimental or numerical, including different system parameters, for instance mass and damping ratios.

Acknowledgments

The Regional Program POR FESR 2014 2020 - 1.3.b - Ricerca e sviluppo - Aree tecnologie marittime e smart health of Regione Friuli-Venezia Giulia is acknowledged for providing the financial support of the SOPHYA Project.

References

- Bearman, P., 1984. Vortex shedding from oscillating bluff bodies. *Annu. Rev. Fluid Mech.* 16 (1), 195–222.
- Bearman, P., 2011. Circular cylinder wakes and vortex-induced vibrations. *J. Fluids Struct.* 27, 648–658.
- Bernitsas, M.M., Raghavan, K., Ben-Simon, Y., Garcia, E., 2008. VIVACE (Vortex Induced Vibration Aquatic Clean Energy): A new concept in generation of clean and renewable energy from fluid flow. *J. Offshore Mech. Arct. Eng.* 130 (4), 041101.
- Chaplin, J., 1984. Nonlinear forces on a horizontal cylinder beneath waves. *J. Fluids Mech.* 147, 449–464.
- Contento, G., Codiglia, R., 2001. Nonlinear free surface induced pressure on a submerged horizontal circular cylinder at low Keulegan–Carpenter numbers. *Appl. Ocean Res.* 23, 175–185.
- Contento, G., Lupieri, G., Jasak, H., Vukčević, V., 2015. Numerical study of unsteady breaking waves induced by a submerged hydrofoil at steady forward speed. In: NAV 2015 18th International Conference on Ships and Shipping Research.
- Francescutto, A., Contento, G., 1999. Bifurcations in ship rolling: experimental results and parameter identification technique. *Ocean Eng.* 26 (11), 1095–1123.
- Gabbai, R., Benaroya, H., 2005. An overview of modeling and experiments of vortex-induced vibration of circular cylinders. *J. Sound Vib.* 282, 575–616.
- Guilmineau, E., Queutey, P., 2004. Numerical simulation of vortex-induced vibration of a circular cylinder with low mass-damping in a turbulent flow. *J. Fluids Struct.* 19 (4), 449–466.
- Khalak, A., Williamson, C., 1996. Dynamics of a hydroelastic cylinder with very low mass and damping. *J. Fluids Struct.* 10 (5), 455–472.
- Kinaci, O.K., 2016. 2-D URANS simulations of vortex induced vibrations of circular cylinder at Trsl3 flow regime. *J. Appl. Fluid Mech.* 9 (5), 2537–2544.
- Levenberg, K., 1944. A method for the solution of certain non-linear problems in least squares. *Quart. Appl. Math.* 2 (2), 164–168.
- Löhner, R., Yang, C., 1996. Improved ALE mesh velocities for moving bodies. *Commun. Numer. Methods. Eng.* 12 (10), 599–608 Chichester, England; New York: Wiley.
- Lupieri, G., Contento, G., 2015. Numerical simulations of 2-D steady and unsteady breaking waves. *Ocean Eng.* 106, 298–316.
- Lupieri, G., Contento, G., 2017. On the wavy flow past a weakly submerged horizontal circular cylinder at low Keulegan–Carpenter numbers. *J. Mar. Sci. Technol.* 1–21. <http://dx.doi.org/10.1007/s00773-017-0445-y>.
- Marquardt, D., 1963. An algorithm for the least-squares estimation of nonlinear parameters. *J. Soc. Ind. Appl. Math.* 11 (2), 431–441.
- Menter, F.R., 1994. Two-equation eddy-viscosity turbulence models for engineering applications. *AIAA J.* 8, 1598–1605.
- Mittal, N., Mittal, S., 2016. Lock-in in vortex-induced vibration. *J. Fluid Mech.* 794, 565–594. <http://dx.doi.org/10.1017/jfm.2016.157>.

- Morison, J., O'Brien, M., Johnson, J., Schaaf, S., 1950. The force exerted by surface waves on piles. *Pet. Trans.* 189, 149–154. <http://dx.doi.org/10.2118/950149-G>.
- Morse, T., Govardhan, R., Williamson, C., 2008. The effect of end conditions on the vortex-induced vibrations of cylinders. *J. Fluids Struct.* 24, 1227–1239.
- Norberg, C., 2003. Fluctuating lift on a circular cylinder: review and new measurements. *J. Fluids Struct.* 17, 57–96.
- Pan, Z., Cui, W., Miao, Q., 2007. Numerical simulation of vortex-induced vibration of a circular cylinder at low mass-damping using RANS code. *J. Fluids Struct.* 23 (1), 23–37.
- Press, W.H., Flannery, B.P., Teukolsky, S.A., Vetterling, W.T., 1992. *Numerical Recipes in Fortran 77: the art of scientific computing*. Cambridge University Press, New York.
- Sarpkaya, T., Isaacson, M., 1981. *Mechanics of Wave Forces on Offshore Structures*. Van Nostrand Reinhold, New York.
- Vikestad, K., Vandiver, J., Larsen, C., 2000. Added mass and oscillation frequency for a circular cylinder subjected to vortex-induced vibrations and external disturbance. *J. Fluids Struct.* 14, 1071–1088. <http://dx.doi.org/10.1006/jfls.2000.0308>.
- Wanderley, J., Souza, G., Sphaier, S., Levi, C., 2008. Vortex-induced vibration of an elastically mounted circular cylinder using an upwind TVD two-dimensional numerical scheme. *Ocean Eng.* 35 (14), 1533–1544.
- Williamson, C., Govardhan, R., 2008. A brief review of recent results in vortex-induced vibrations. *J. Wind Eng. Ind. Aerodyn.* 96, 713–735.
- Wu, W., Bernitsas, M.M., Maki, K., 2014. RANS simulation versus experiments of flow induced motion of circular cylinder with passive turbulence control at $35,000 < RE < 130,000$. *J. Offshore Mech. Arct. Eng.* 136 (4), 041802.